ICAS 2021 SHANGHAI
International Council of the Aeronautical Sciences
32nd Congress of the International Council of the Aeronautical Sciences
September 6-10, 2021
Pudong Shangri-La, Shanghai, China

INTEGRATION OF FUSELAGE-MOUNTED OVER-WING ENGINES ON A MID-RANGE AIRCRAFT

Patrick Wegener

German Aerospace Center (DLR), Lilienthalplatz 7, 38108 Braunschweig

Abstract

For conventional transport aircraft configurations, the clearance below the wings for large-diameter UHBR engines is limited. A configuration with engines located above the wing enables the integration of large-diameter UHBR engines with high propulsive efficiency and consequently holds potential for overall drag improvements if a favorable integration concept can be elaborated. Moreover, noise benefits utilizing the shielding effect of the wing are conceivable. Within the framework of the German LuFo V project AVACON (AdVanced Aircraft CONcepts), configurations with this type of engine arrangement were investigated. For the present variant, the structural connection to the aircraft is made via a horizontal pylon to the top of the fuselage. In order to be able to investigate the complex aerodynamic interactions between engine and wing upper surface, RANS CFD simulations were performed using the DLR TAU code with a SA turbulence model. Based on an engine positioning analysis, the geometry of the pylon was iteratively designed and engineered in detail. Subsequently, the geometry of the wing was adapted to the flow condition resulting from the engine integration by optimizing the twist and upper surface shape. Results show positive installation effects in terms of total drag due to the interaction between pylon, nacelle, and wing. The effects are closely connected and partly counteracting: Benefits in the drag components of the nacelle have a negative effect on the component drag of the wing and vice versa. In general, the influence of the geometry parameters on the overall drag and their interacting influence is more prominent in such a configuration than in a conventional engine setup. The use of advanced optimization methods is therefore crucial for a successful design.

Keywords: Unconventional configurations, UHBR Engine, Over-the wing mounted engines

1. Introduction

The development of new aircraft is driven by two factors: a reduction in noise and an increase in efficiency. On the engine side, the latter can be increased by means of a higher bypass ratio, which is also accompanied by an increase in engine diameter. For this reason, there are limits to this approach in a classic under-wing engine configuration, like the required landing gear length. An over-wing configuration would not be limited in this regard, and would have the potential to achieve further advantages in terms of noise emissions due to the shielding effect of the wing. The interference of the engine with the local supersonic regions on the upper side of the wing creates complex flow situations, which is why the implementation of these concepts in practice has so far only been carried out in isolated cases.

The topic has been the subject of past research: The primary aim of the work by Bodersen et al [1] was noise shielding. One of the results was that the engine position in front of the leading edge of the wing causes negative aerodynamic interferences. Hooker et al [2] simulated practically all conceivable engine positions with similar results for this position. Their work shows a favorable position near the trailing edge of the wing. For a business aircraft, Fujino [3] documented the development of a configuration with this kind of engine position, which resulted in a commercial product.

The national “Luftfahrtforschungsprogramm” (LuFo) V funded project AVACON takes this work up with the aim of a broader assessment of such a configuration. In the framework of preliminary work, Wöhler [4] developed a reference configuration with a high-aspect ratio wing and ultra-high bypass engines for the “middle of the market” segment (Figure 1) with a mission range of 4600nm carrying 257 Passengers using low-fidelity preliminary design methods.

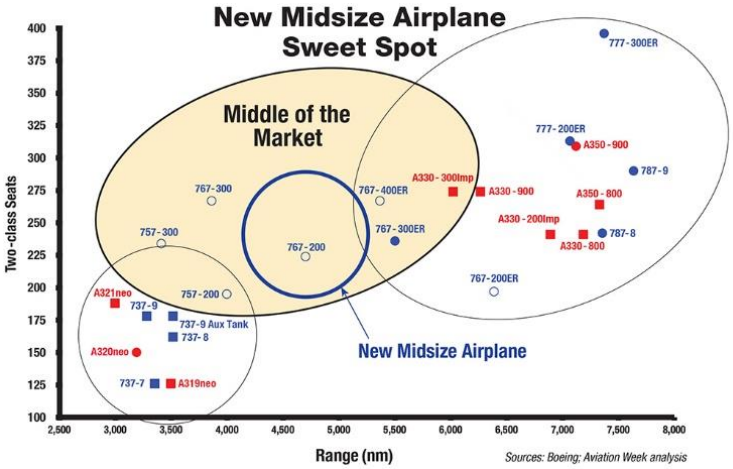

Figure 1 - the 'Middle of the market' segment

For this aircraft, a wing was designed with high-fidelity CFD methods as a wing-body configuration for the given cruise point [5]. In the framework of the AVACON project, three engine-mounting concepts were investigated:

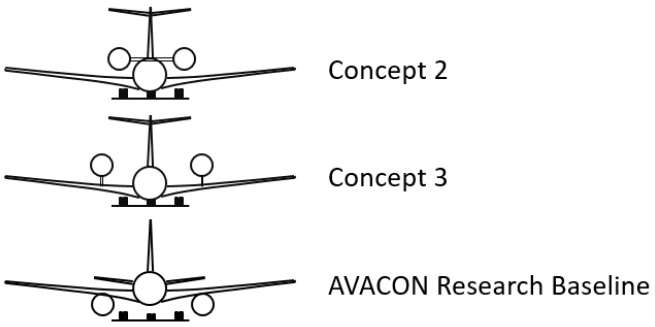

Figure 2 - AVACON Engine configurations

In Concept 2, the engines are mounted on a pylon in the form of a stub wing on the top of the fuselage. This enables an undisturbed air flow in the area between the underside of the engine and the wing. Furthermore, the design of the high-lift system is not constrained by engine elements. One disadvantage of this configuration is the fuselage structure, which has to be designed in a more complex way to support the engine loads. In this context, Concept 3 can make use of the wing's spar structure, while the fuel supply also does not have to be routed through the cabin. On the other hand, in this configuration the pylon is located closer to the sensitive area between the nacelle and the upper surface of the wing, which is expected to result in higher interference drag.

To evaluate the two concepts, the AVACON Research Baseline provides the reference in the form of a classic configuration. For consistency of use within the AVACON project, the nomenclature is not continuous at this point. In all cases, a UBR engine with a bypass ratio of 16.3 is utilized, with geometry provided by a consortium partner. The present work focuses in detail on the Concept 2 configuration.

Figure 3 gives an impression of the geometry and dimensions:

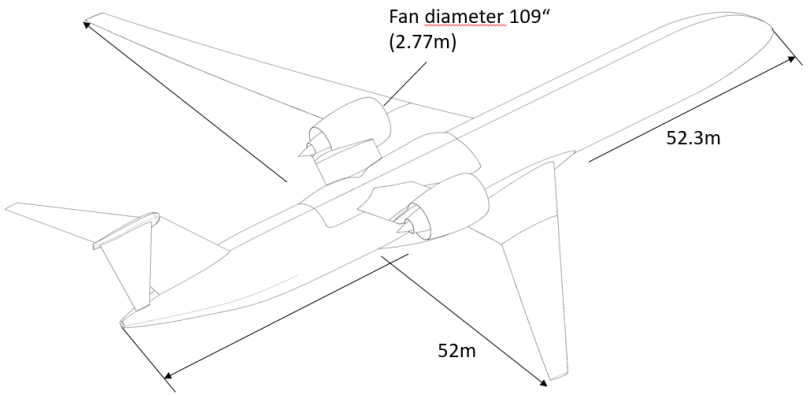

Figure 3 - AVACON Concept 2 Geometry

2. Process chain

The current investigation is based on a process chain starting from the geometry creation via mesh generation to numerical simulation. This chain could be implemented in a fully automatized optimization process or utilized as semiautomatic assistance for an accelerated workflow.

The essential starting point for CFD simulations is the availability of a detailed and robust geometry. For the present investigation, a parameterized geometry in CATIA V5 was used. For simplicity - since the focus is on the interference effects between engine and wing - the simulations are performed without the empennage. For the investigation of the over-wing engine configurations, the wing position of the reference configuration [5] was shifted backward by three fuselage frames to compensate for the expected center of gravity shift compared to a conventional underwing engine installation.

Ensuing from the aircraft geometry generated in CATIA V5 [6], the grid generator Centaur by CentaurSoft was used. On the surface, this tool enables the creation of hybrid grids composed of triangles or quadrilaterals. Originating from the surface discretization, a near surface grid is created consisting of prisms and hexahedrons. The near-field grid is characterized by a first wall spacing, stretching ratio in surface normal direction and number of layers. An overview of these global parameters and the resulting mesh properties is listed in Tab. 1.

Number of boundary nodes	~0.58 mil
Initial layer thickness	0.00487mm
Stretching ratio (Prims)	1.23
Number of prism layers	43
Number of prisms	~21 mil
Number of pyramids	~0.1 mil
Number of tetrahedrons	~17 mil

Table 1 - Grid parameters and properties for WBE

The remaining volume is filled by tetrahedrons. Local refinements of surface and tetrahedral cells are achieved by using the method of CATIA-to-Centaur Sources (CCS) to enable a reconstruction of similar grids in spite of geometry adaptations like an engine position variation. This method was already applied to various aircraft configurations [5] [7] [8].

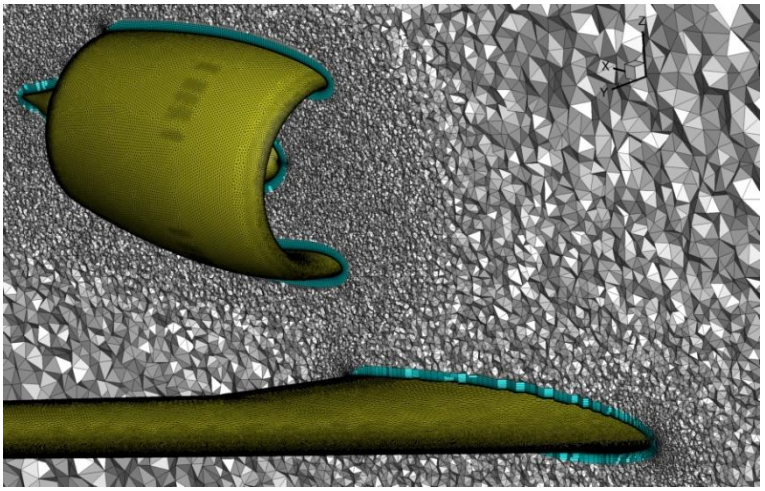

Figure 4 - CFD Mesh example

An impression of the grid is given in Figure 4. The prism layer is colored in blue and the unstructured cells are marked grey.

The numerical simulations were obtained using the DLR TAU-code. This CFD solver is based on an edge-based finite-volume approach solving the compressible, three-dimensional Reynolds averaged Navier-Stokes equations [9]. For these particular simulations the Spalart-Allmaras one-equation eddy viscosity model [10] enhanced by the negative formulation [11] is utilized. The spatial discretization was realized by a 2nd order accurate central scheme in combination with the implicit LUSGS scheme for time stepping. The artificial dissipation is composed of a combination of matrix (80%) and scalar (20%) dissipation. A detailed analysis of the drag components is achieved with the aid of the surface-based drag evaluation tool AeroForce [12]. In addition to a component wise breakdown of pressure and friction drag, spanwise load distributions can be extracted.

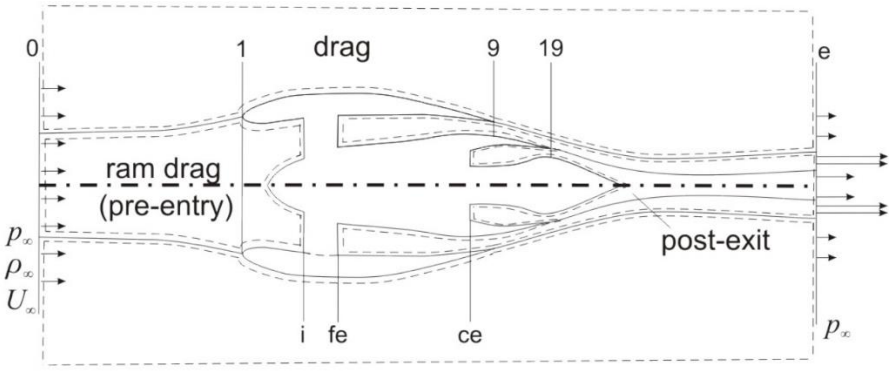

Figure 5 - Thrust-Drag Bookkeeping

In the course of the work, the focus is on the aerodynamic drag, in particular of the subcomponents. This involves accounting for the thrust and drag components as accurately as possible. For this purpose, force components within the engine stream tube (thrust) are separated from force components acting on the outer geometry (drag) (Figure 5).

For detailed analysis, the drag is further subdivided into components, such as fuselage, wing, nacelle and pylon surfaces. Figure 6 shows the boundaries of the components:

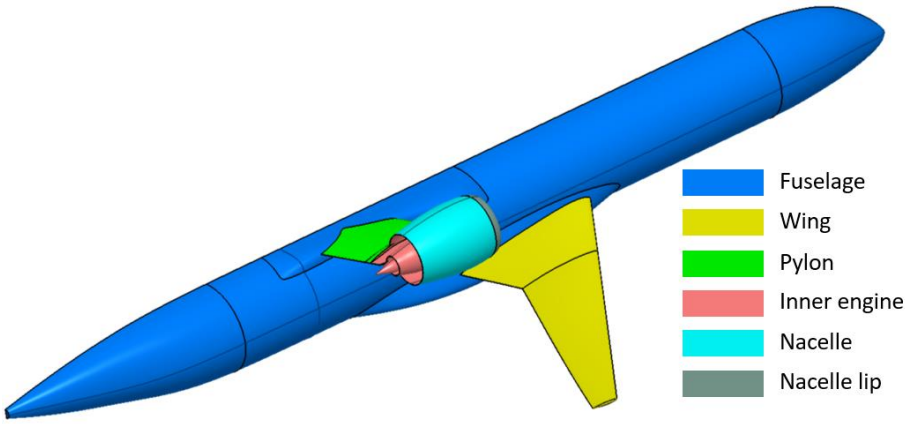

Figure 6 - Boundaries of the drag components

While the inner engine is always part of the engine stream tube, the nacelle lip will be split on the engine stagnation line: the outer part will be accounts for the outer geometry while the inner part belongs to the stream tube.

The geometries of the configuration - especially the pylon surfaces - are initially modeled by manual iterations using CATIA. Subsequently, these are optimized using DLR's own 'Powerful Optimization Tool' (POT) by Wilke [13] in a single-fidelity surrogate model-based approach. The overall process can be divided into three phases:

1) Design of Experiments (DoE)
2) Surrogate modeling
3) Optimization

Initially, a design of experiments needs to be carried out to explore the parameter space by a defined number of samples. For this case, an advanced Latin Hypercube, the Central Voronoi Tessellation was used to define the parameter combinations. The surrogate model is generated with the aid of a kriging model [14]. Subsequently, the optimization is started from the original surrogate model. The optimizer not only aims for an optimum, but also improves the surrogate model by applying an adaptive sampling strategy. Therefore, a hybrid optimization approach was used, which is composed of a Differential Evolutionary (DE) algorithm and a non-gradient based simplex pattern search method. By this approach, global regions of interest are identified by the DE, while the pattern search more accurately determines the local optimum in these regions.

Mission planning was performed as part of the aircraft preliminary design. For the cruise flight, 3 segments of different lift coefficients and flight altitudes are planned. The longest cruise flight segment was defined as the operating point for the aerodynamic simulations carried out in the following. The lift coefficient C_A is 0.5, the Mach number 0.83 at a flight altitude of 37,000ft. The angle of attack is continuously adapted during the simulation to retain the prescribed lift coefficient.

Thrust is modeled by the engine boundary condition, assuming the following pressure and temperature conditions:

	Pressure ratio P_t/p_0	Temperature ratio t_t/t_0
Fan	2.022	1.08
Core	1.7020	2.43

Table 2 – Engine boundary conditions

For continuity reasons, the intake mass flow was modeled as the sum of the core and bypass outlet mass flow.

3. CFD Simulation

Figure 7 shows the simulation sequence:

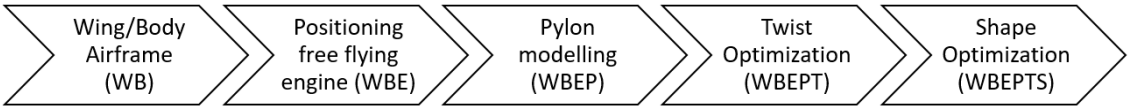

Figure 7 - The simulation workflow

The surfaces of the model are grouped into wing (W), body (B), engine (E) and pylon (P) for component-wise evaluation of the partial drag. The abbreviations are used in the following as nomenclature. Starting from a wing-body airframe (WB), the spatially dependent interference effects between engine and wing are identified in the next phase by positioning the engine without any pylon in the trailing edge vicinity of the wing (WBE). As a result, a position for the subsequently modeled pylon (WBEP) is obtained. This configuration is then used to optimize the wing geometry in order to adapt the wing aerodynamics to the effects caused by the engine. In order to enable a correlation of the observed effects to the design parameters of the wing, the optimization of twist distribution and airfoil shape is performed sequentially. This is based on the assumption that the interactions between both parameter groups are sufficiently small. In the first step, the twist distribution is optimized with the wing profiles unchanged, followed by an optimization of the wing profiles using the resulting twist distribution. The nomenclature used for these phases is 'WBEPT' for the twist and 'WBEPTS' for the shape optimization.

3.1 Engine Positioning

The engine geometry was positioned in a cuboidal parameter space above the wing (WBE configuration). In this way, a preselected positioning above and behind the trailing edge of the wing was taken into account. The variable parameters consisted of the spatial coordinates x,y and z, each dimensionless in relation to the mean aerodynamic chord of 5.277 m. The dimensions of the parameter space are shown in Tab.2.

Parameter	Lower limit	Upper limit
X	-0.2	0.2
Y	0.85	1.5
Z	0.1	0.4

Table 3 – WBE Parameter space

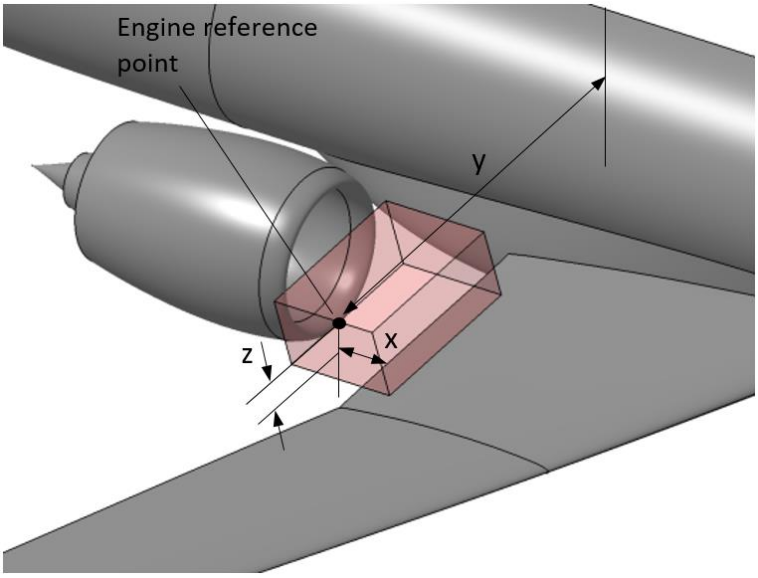

Figure 8 - Engine Positioning

The foremost point of the lower (“6 o`clock”) section through the inlet lip was chosen as the reference point for translation (Figure 8). The objective of the optimization was to determine the engine position

of the minimum total drag as well as the generation of surrogate models of the drag components of the wing, fuselage and nacelle.

A surrogate-model-based optimization was performed, in which 30 iterations were simulated for the design of experiments (DOE), followed by a total of 55 iterations for the optimization of the total drag.

Compared to the WB configuration, this also confirms an effect that has already been described in the literature [2],[5]: For such a configuration, the decelerating effect of the engine on the inlet flow affects the aerodynamics of the upper wing surface of the inner wing, thus reducing lift in this area.

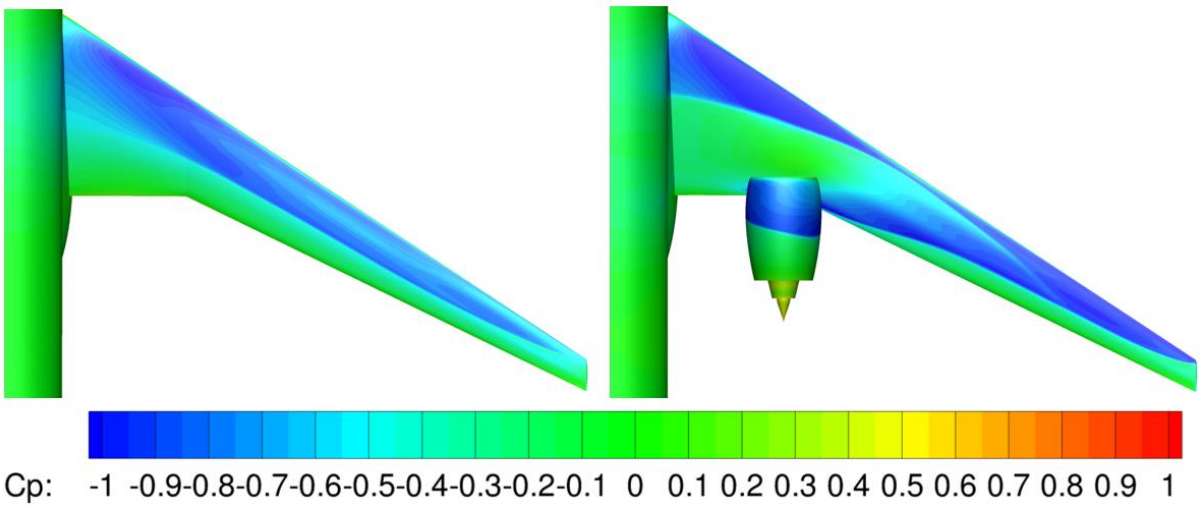

Figure 9 - Engine effect on wing pressure distribution

To satisfy the boundary condition of constant CA=0.5, the angle of attack is increased by about 1°. This results in more lift being generated in the outer wing. As indicated on the right side of Figure 9, the shock in the inner wing is amplified and shifted forward. The total drag of the configuration increases by 16-50% depending on the position.

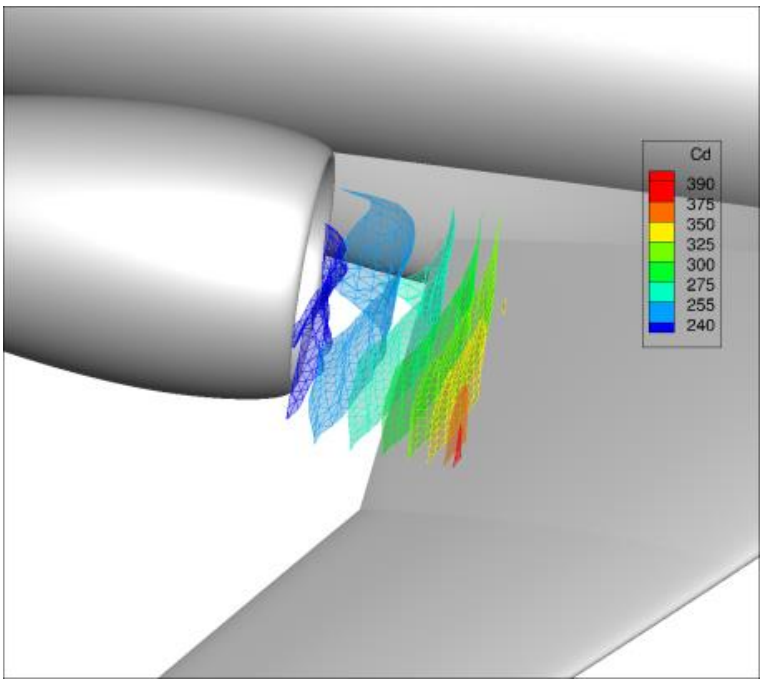

Figure 10 - Spatial distribution of the total drag

Figure 10 shows the spatial distribution of the total drag as iso-drag surfaces. The engine is shown at an exemplary position for orientation. The surfaces refer to the envelopes of the engine reference point at the same drag. A clear dependence of the drag on the engine position can be observed, with a significant reduction with increasing distance from the wing.

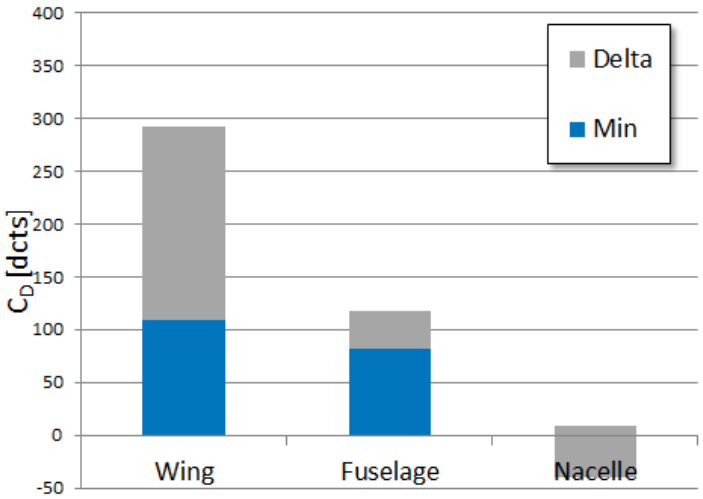

Figure 11 - Distribution of the drag components

Figure 11 shows an overview of the distribution of the drag components over all simulations carried out in the DOE. A clearly larger variation of the wing drag values is apparent than for the fuselage. Furthermore, the effect of negative partial drag values of the nacelle can be observed, which is known from the literature [5], [2].

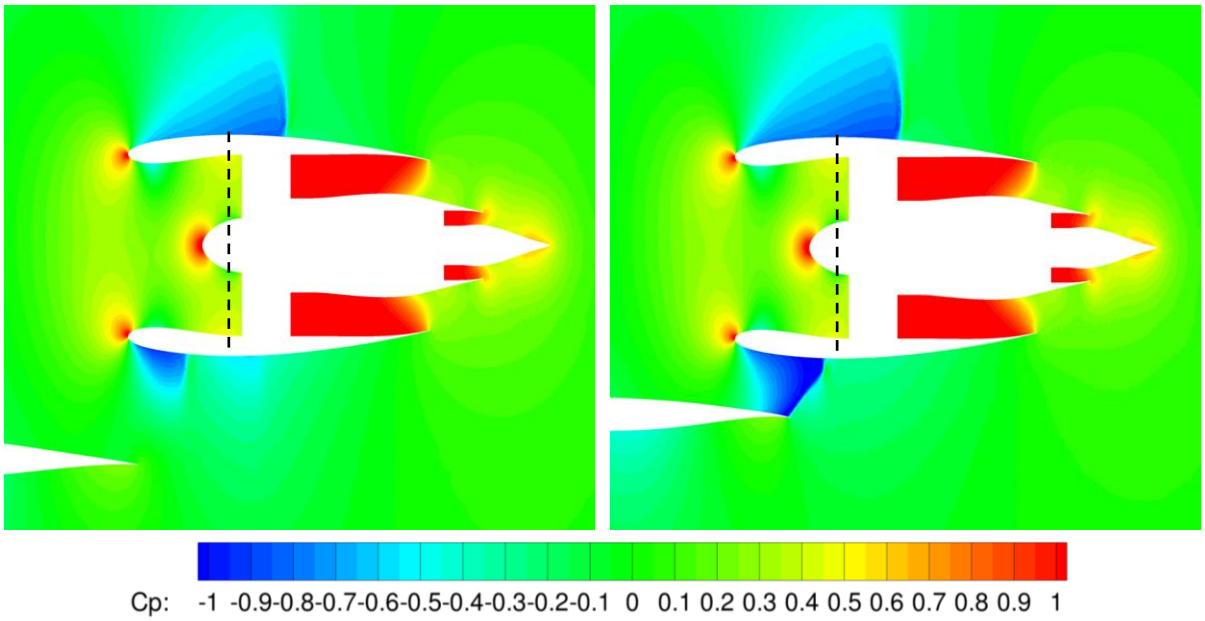

Figure 12 - Comparison of two nacelle positions with negative partial drag

Figure 12 shows the underlying effect: The position of the thickest point of the nacelle outer contour is plotted as a dashed line. It can be seen that on the upper side of the nacelle the low-pressure area changes only marginally with a changed engine position. In addition, the extent of this area exceeds the thickest part of the nacelle profile. On the lower side, however, the low-pressure area is strongly influenced by the upper side of the wing and ends in front of the thickest point. The lower pressure acts on surfaces with forward surface normals and thus creates a forward suction that reduces the partial drag of the nacelle.

On the right figure, shock and minimum pressure coefficient of the lower nacelle side are much more distinct. For this case, the partial drag of the nacelle shows significant negative values. However, the wave drag is also considerably increased for this position, which leads to an increase of the partial drag of the wing.

Figure 13 shows the iso-drag surfaces for the drag components of nacelle and wing. Analogous to Figure 10, a nacelle in an exemplary location is also shown here for spatial orientation. Two opposite effects can be observed:

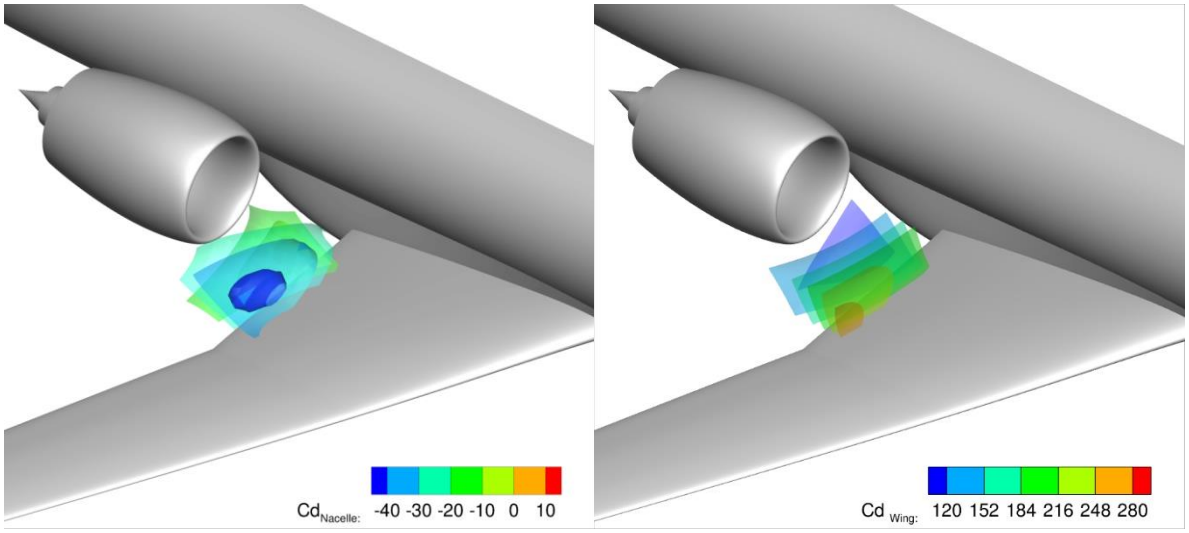

Figure 13 - Comparison for partial nacelle and wing drag

On the one hand, there is a spatially defined area where the minimum of the component drag of the nacelle can be found, recognizable by the blue cloud above the airfoil kink. On the other hand, this is the same area where the largest drag increase on the wing is observed, recognizable by the red areas in this area in the right part of the figure. Both effects thus correspond in a negative way, since the magnitudes of the degradation on the wing overcompensate for the positive drag effects of the nacelle.

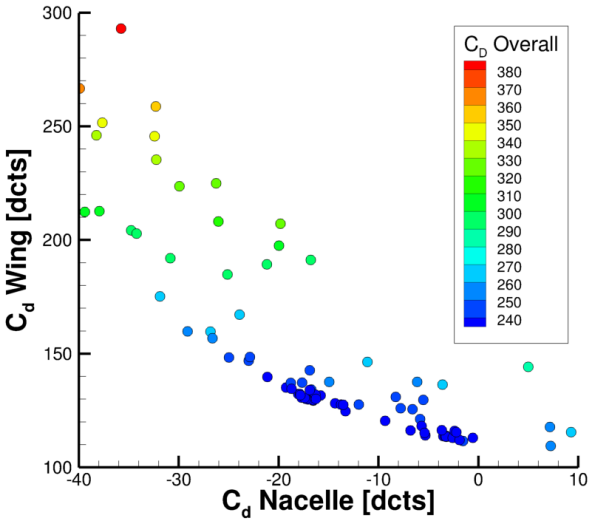

Figure 14 - Ratio $C_{d,\,Nacelle}$ to $C_{d,\,Wing}$

Figure 14 shows the results in two dimensions: Shown on the horizontal axis is the nacelle drag, while the component drag of the wing is plotted vertically. One can see a correlation of increasing wing drag for decreasing values of nacelle drag. Furthermore, this evaluation with unchanged wing alone already shows a wide range of solutions. Consequently, the goal of the wing optimization becomes to minimize the negative drag effects on the wing while maintaining the suction effect on the nacelle.

3.2 Pylon modeling

For further investigations, the engine position was determined taking structural considerations into account:

In vertical direction, this position is limited by the constraint that the upper fuselage contour should not be increased. Furthermore, a minimum height is defined for the pylon spar which is orientated exactly horizontal. In spanwise direction, a maximum dimension was determined for which the bending moments in the pylon remain within reasonable limits. Based on the position variations, a position with a slight overlap of the trailing edge was chosen where the nacelle component drag shows negative values.

At the selected position, the pylon was designed as a swept stub wing in a manual iteration. The initially varied parameters are outlined in Figure 15:

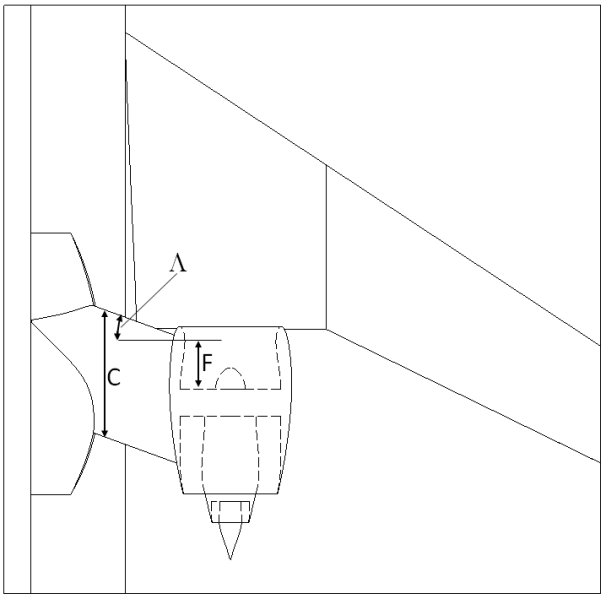

Figure 15 - Pylon design

Starting on the nacelle from the distance F to the fan plane, a untapered, swept wing with a symmetrical airfoil of chord length C was built from the nacelle to the fuselage with the sweep angle Λ. At the intersection with the fuselage, a fairing was modeled to smoothen the transition.

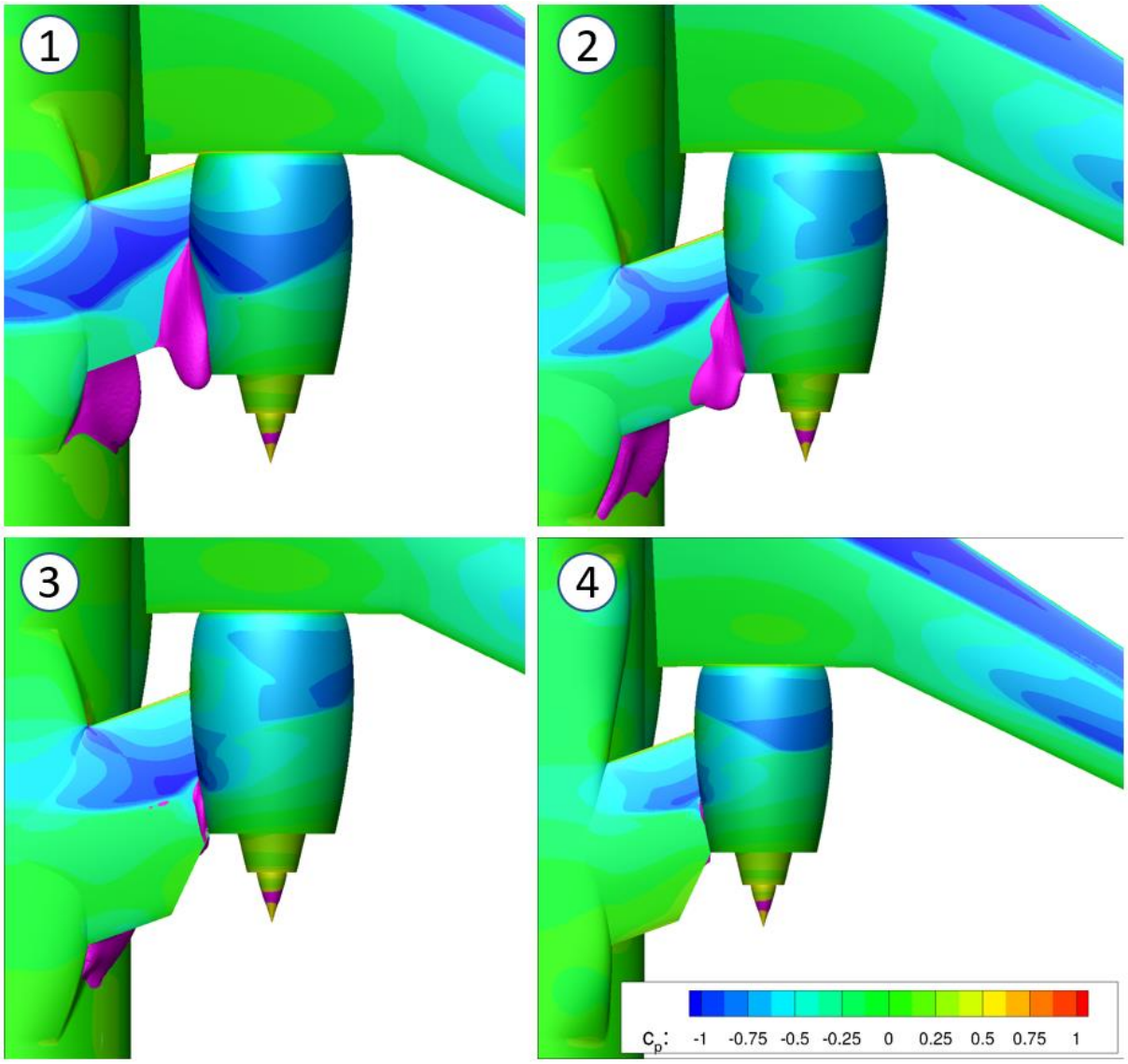

Figure 16 – Stages of pylon iteration

In the subsequent simulation, shock-induced separations occurred both on the pylon upper side in the region of the intersection with the engine nacelle and on the lower side at the fairing. These separations could be gradually reduced and finally avoided by a manual iteration. Figure 16 shows examples of the process, with separation regions defined by v_x < -1m/sec, highlighted in magenta. The separations on the nacelle side could be avoided by a consistent reduction of the pressure gradient in flight direction. This was achieved by

1. forward sweep (Λ = -20°)
2. a recessed leading edge (F=7.2% MAC)
3. an increase of the chord length (C= 85% MAC)
4. an extension of the fuselage/pylon fairing

To avoid separations on the lower side, the fuselage fairing was extended over the wing and given a waisted design. It thus acts as a transonic displacement body and reduces the disturbing effect of the nacelle on the flow.

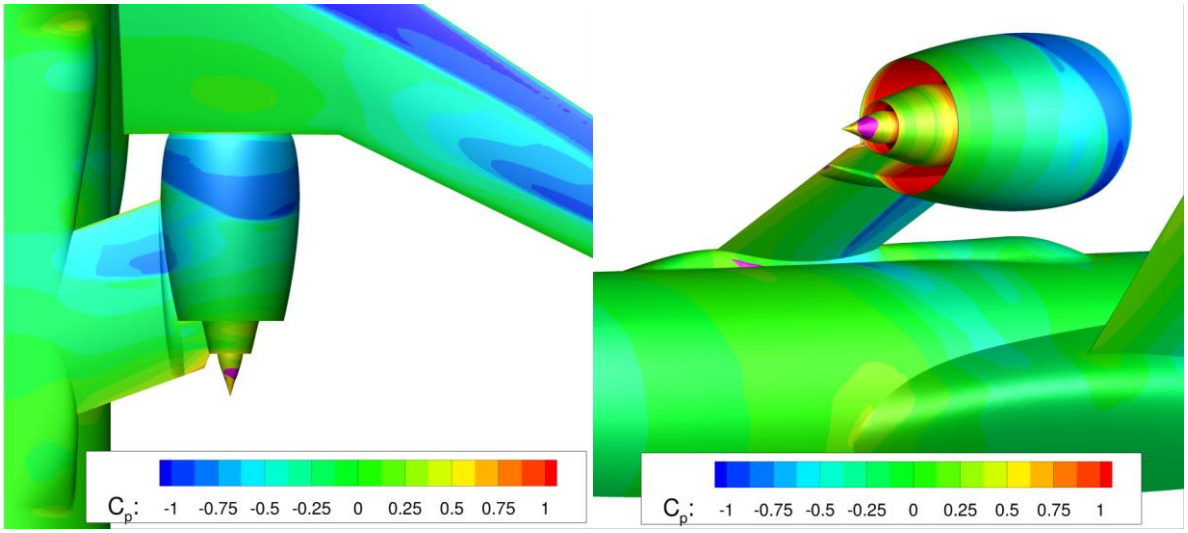

Figure 17 – The final pylon geometry

The final pylon shape is displayed in Figure 17: as a last step, the pylon was extended to the engine core and a fairing was introduced to smoothen the intersection between pylon and engine.

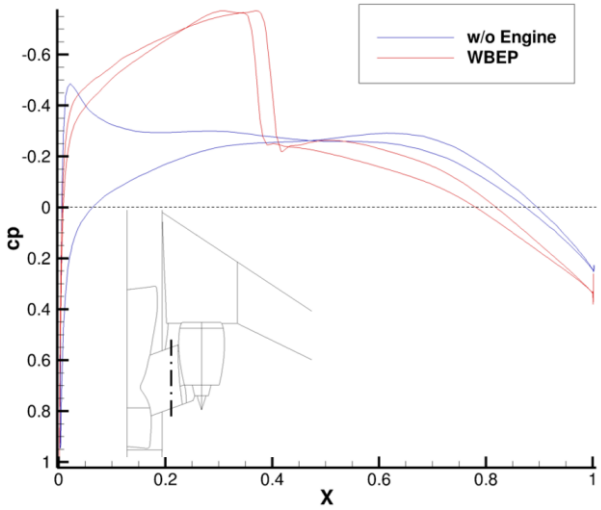

Figure 18 - Pylon pressure distribution

As already found on the nacelle, a negative partial drag was also observed on the pylon. To analyze this, a simulation was carried out without the engine. Comparing the two pressure distributions (Figure 18), the low-pressure area can be seen, whose shock position is also located in front of the thickest part of the airfoil. With these measures, the pylon geometry was completed, and further focus was placed on the optimization of the wing.

3.3 Wing optimization

3.3.1 Twist distribution

A 5th order Bezier curve is used internally to define the twist distribution. This is shown in blue in Figure 19. The underlying control points are shown as a polygonal curve.

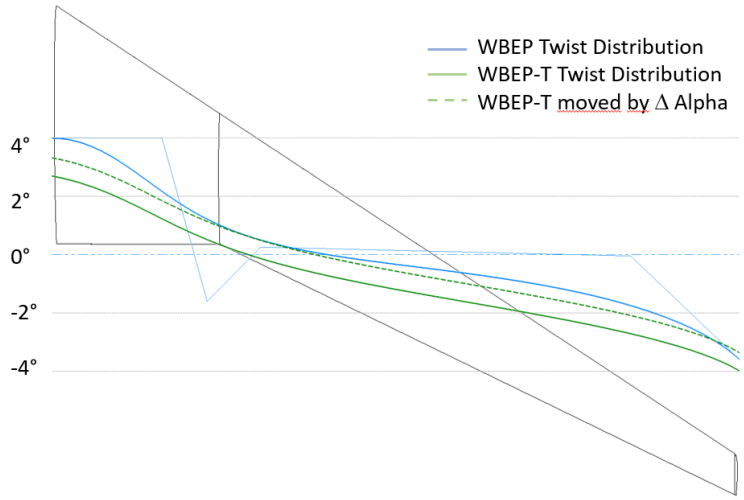

Figure 19 - Twist distribution

As a degree of freedom for optimization, a parameter space of vertical modification of +/-2° was released for each of the 6 control points. A DOE with 60 iterations was used to form the surrogate model, followed by optimization with 20 iterations. The optimization criterion was total drag minimalization.

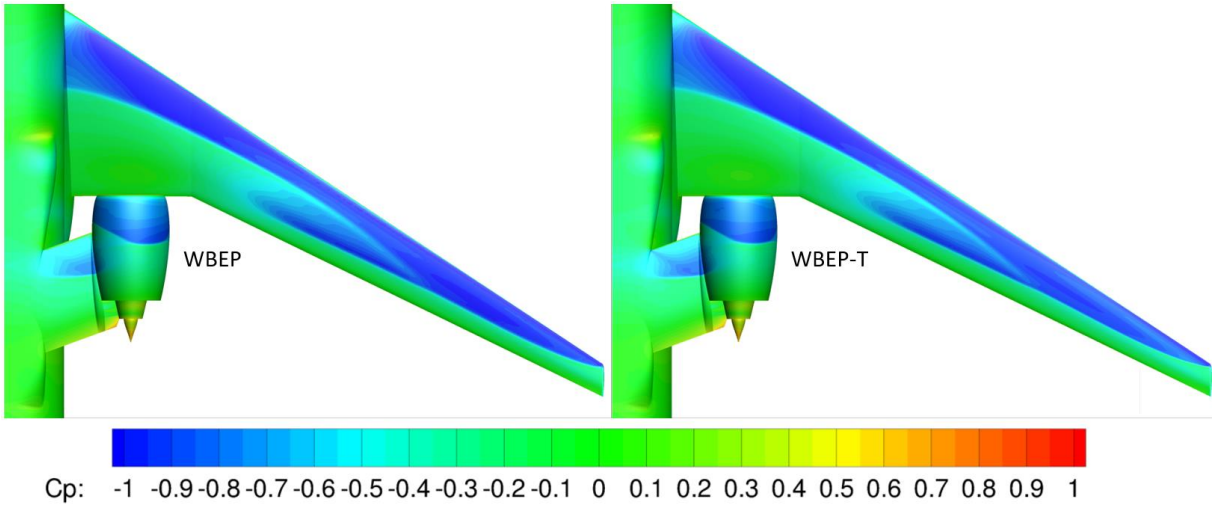

Figure 20 - Pressure Distribution changes after twist optimization

Figure 20 shows the pressure distribution after twist optimization. It is evident that the forward shift of the shock observed in Figure 9 has not changed significantly as a result of the twist optimization.

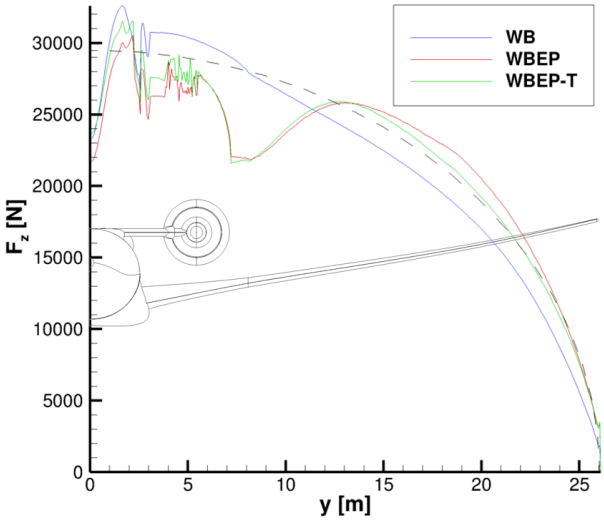

Figure 21 - Spanwise lift distribution after twist optimization

Figure 19 shows the result of the twist optimization. It can be seen that, in a first approximation, the complete twist distribution curve was shifted towards lower twist values reducing the incidence angle of the wing. To achieve the boundary condition of C_A=0.5, the angle of attack was then increased during the simulation. In the same figure, the new twist distribution shifted by the amount of the change in angle of attack is shown as a green dashed curve. Compared to the initial situation, differences can be seen in the inner and outer regions, while in the region of the kink the curves are nearly identical. By increasing the angle of attack, fuselage, pylon and engine nacelle generate more lift, while less lift is generated in the outer wing due to the reduced twist. Both effects result in a lift distribution getting closer to the elliptical lift distribution, especially in the outer wing section (Figure 21).

3.3.2 Shape optimization

Figure 22 shows an example of the differences in the flow situation caused by the addition of the engine.

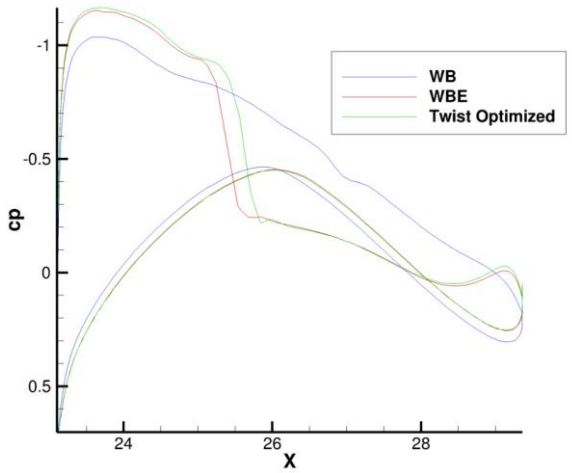

Figure 22 - Pressure distribution at the engine position (y=21.1%)

On the lower side, the flow is only slightly affected; the difference between WB and WBEP arises from the different angle of attack to achieve the lift coefficient. This becomes particularly clear when comparing the situation before and after the twist optimization: the curves of the bottom side of WBE and WBEPT are almost identical. On the upper side, the differences due to the addition of the engine are clearly visible (WB compared to WBE). For this reason, the optimization of the wing profile is limited to the upper curve.

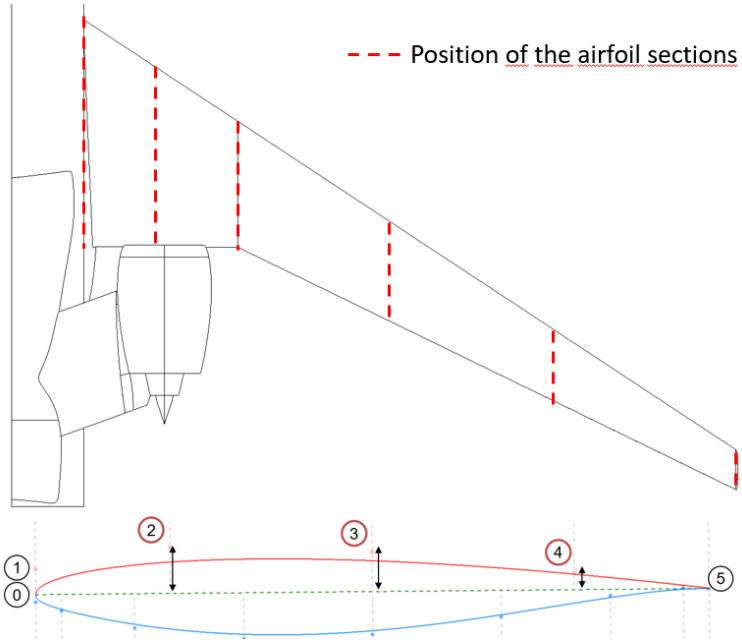

Figure 23 – Positions and Bezier curve of the airfoils

The surfaces of the upper wing shape are modeled using a total of 6 Bezier curves of 5th order (Figure 23). Their 0th and 1st as well as the 5th control point remain unchanged to ensure the connection of the lower contour and the trailing edge, respectively. As input variables for optimization, the vertical positions of the 3 remaining control points are varied. Assuming that the engine influences have decayed to the wing tip, the airfoil of the wing tip remains unchanged. The optimization thus includes 15 parameters. A DOE with 150 iterations followed by an optimization with 20 iterations was performed.

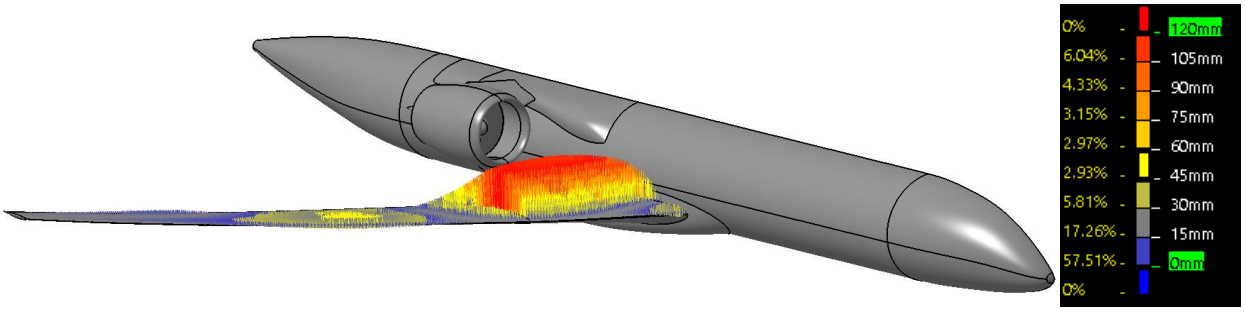

Figure 24 - Geometric change and distribution

Figure 24 shows the normal vectors of the shape optimization result compared to its initial position in 16x magnification. A clear increase in thickness can be seen in the area of the inner wing. In the outer wing area, the resulting wing profile is slightly thinner than the initial position.

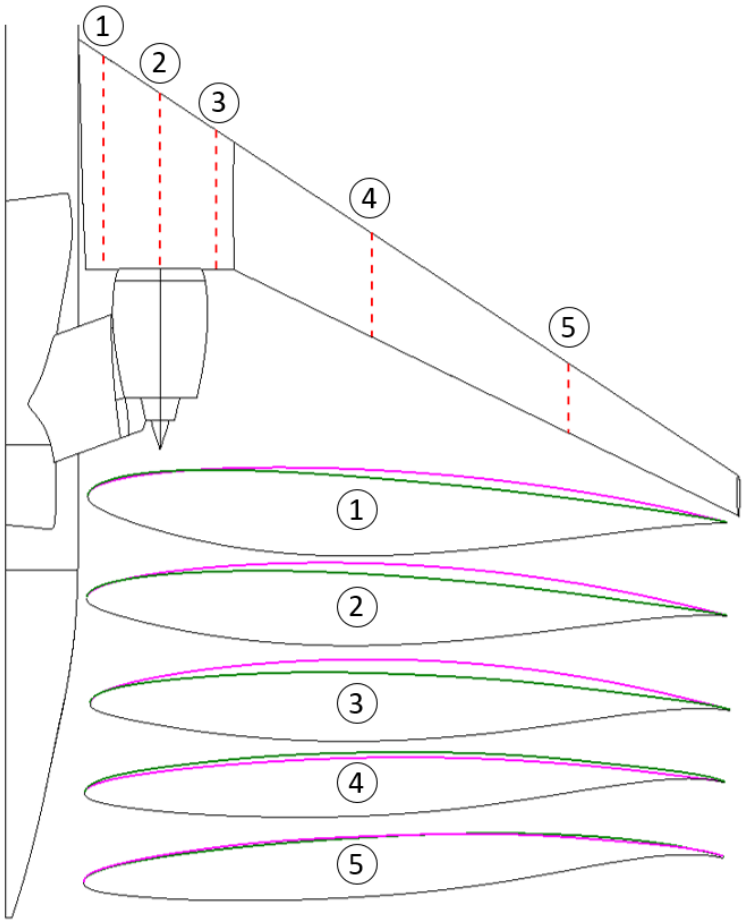

Figure 25 - Airfoils WBEP-T and WBEP-TS

A more detailed insight into the modification of the airfoil profiles is given in Figure 25: In the three inner airfoil sections, the thickening occurs in the rear part of the airfoil, which leads to an increase of the boattail angle. In the outer airfoils, on the other hand, the airfoil thickness is slightly reduced, which contributes to a reduction of the lift in the outer wing.

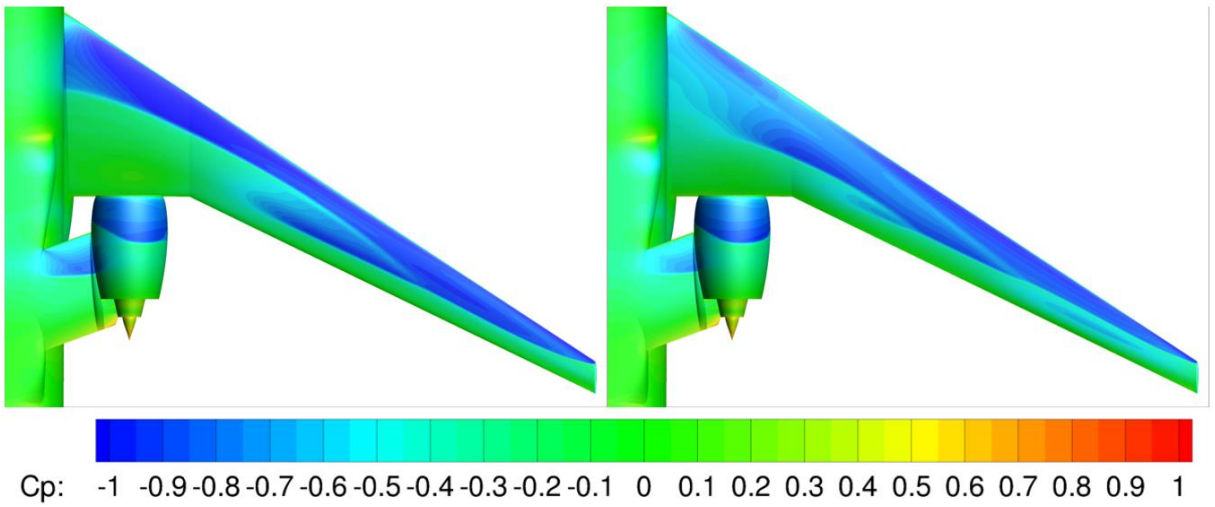

Figure 26 - Pressure Distribution changes after shape optimization

Figure 26 shows the pressure distribution before and after profile optimization. By changing the profile, the position of the shock could be shifted further back again. The minimum pressure coefficient was reduced. In total, more lift is generated in the inner wing, which also brings the pressure distribution closer to the elliptical lift distribution.

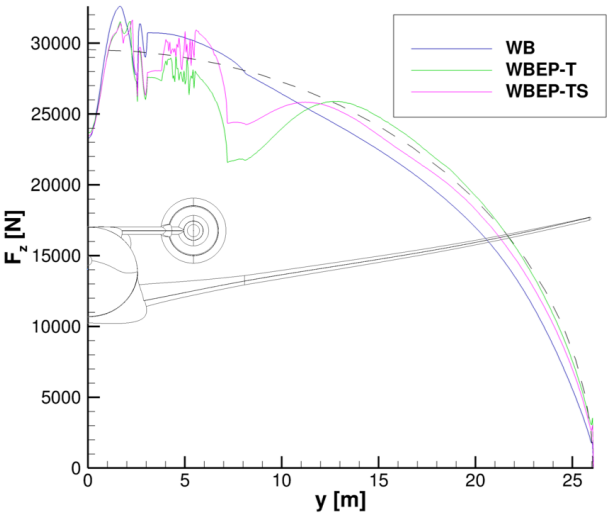

Figure 27 – Lift distribution influence of the shape optimization

Comparing figures Figure 21 and Figure 27, it is apparent that, in contrast to the twist change, the shape optimization was effective in significantly increasing the lift in the area just outboards of the engine (y>7m).

In Figure 28, the change of the major drag and lift components over all simulation phases is shown. It can be seen that the sequential addition of the nacelle and pylon (WB > WBE) increased the total drag, as the positive contributions from the nacelle and pylon were overcompensated by the remaining components. On the lift side, adding the engine reduces the lift component of the fuselage, so that the lift component of the wing increases. Due to the local angle of attack, the pylon generates lift (WBEP phase). This helps to further reduce the lift of the wing. On the drag side, the more complex geometry leads to a further increase in total drag. As an effect of the twist optimization (WBEPT case), a slight reduction of the total drag can be observed, with a major reduction of the wing drag. The drag of the nacelle and pylon components increase slightly. On the lift side, it can be seen that the partial lift of the nacelle and pylon was increased after twist optimization, which - since the total lift remains unchanged - leads to a significant reduction in the lift component of the wing.

$$C_{W_i} = kC_A{}^2 \tag{1}$$

In general, the induced drag is influenced by the factor k which includes effects of lift distribution and aspect ratio and the lift coefficient (1). Since improvements on both parts could be made, the main cause of the reduction in wing drag is due to this effect. For this reason, no significant difference can be seen in the pressure distribution.

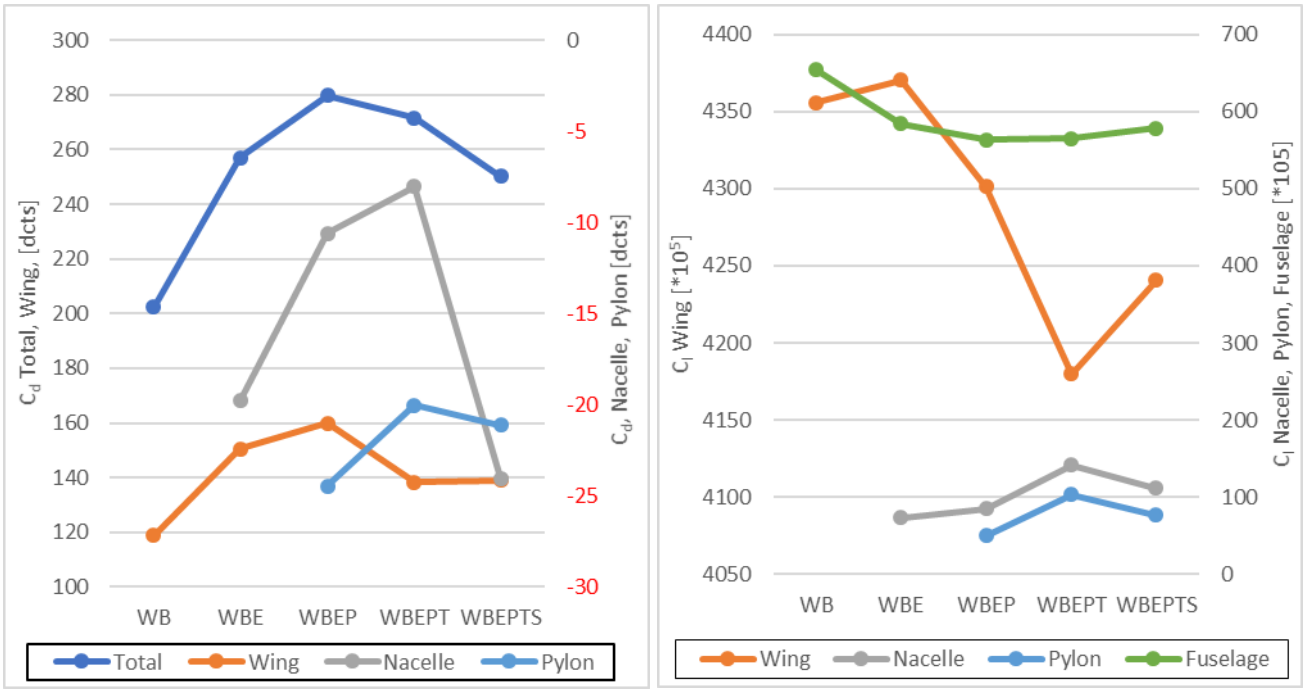

Figure 28 - Drag and lift components in the course of simulation

Comparing the figures Figure 25, Figure 26 and Figure 27 with respect to the influences of the shape optimization (WBEPTS), it is noticeable that the wave drag could be reduced and the lift distribution further improved. On the coefficient side, it is noticeable that the drag component of the wing remains largely unchanged in this step, while the components of the pylon and in particular the nacelle decrease significantly. On the lift side, it can be seen that the wing generates more lift again due to the change in the wing profiles resulting in an increase in camber, while the contributions of the nacelle and pylon decrease. The increase in the lift component of the wing leads to an re-increase in the induced drag (1). Although the wave drag and lift distribution improvements contributed to an improvement in the factor *k*, this effect together with the increase in pressure drag due to the increased airfoil thickness compensates the improvements.

As illustrated in Figure 25, a significant increase in the boattail angle in the area of the airfoil sections upstream of the engine can be seen from the change in airfoil shape. The resulting change in the incoming flow to the underside of the nacelle reinforces the effects of the low-pressure region that has been established:

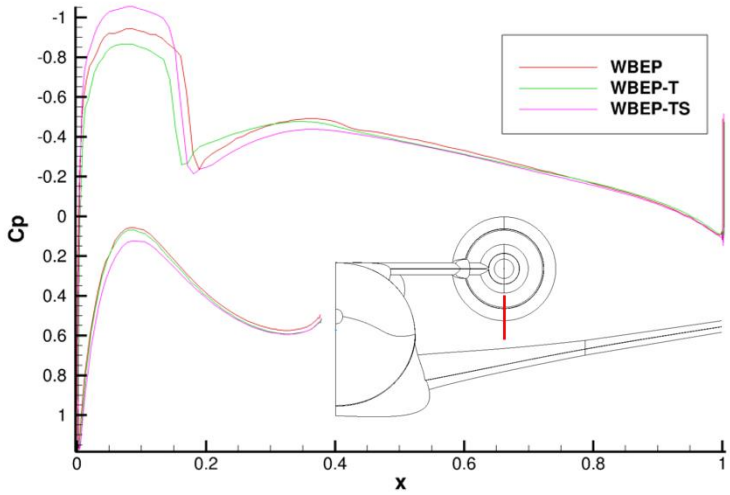

Figure 29 - Pressure distribution of the lower nacelle section in the course of the wing optimization

The positive interference effect amplified in this way contributes to reduce the overall drag significantly.

4. Conclusion

In this paper, the aerodynamic design of an aircraft with UHBR engines located above the wing was described and the influences of pylon design, twist and shape optimization were analyzed. There is a close aerodynamic interaction between the components, which is manifested in the partial drags; in particular, there is an opposing influence between the nacelle outer surface and the wing. In general, the presence of the engine has an upstream influence on the wing, which causes a forward shift and amplification of the shock. In the gap between the upper surface of the wing and the lower surface of the nacelle, a suction effect can develop which has a positive effect on the overall drag. To mitigate the negative influence of the engine on the wing, it has proven advantageous to have the pylon and nacelle generate lift. The wing optimization has led to a thickening of the inner wing and an increase of the boattail angle, which has shifted the position of the shock further downstream. At the same time, the drag component of the nacelle was further reduced. Especially when using engines with extremely high bypass ratios, such a configuration can be beneficial. Compared with the reference configuration of the AVACON project, no overall improvement in total drag was achieved for this configuration. However, in the work of the consortium, especially the engine design, it has been shown that further mutual interferences exist. A competitive design of such a configuration appears only possible by means of complex optimization procedures including all components in a simultaneous way, requiring to substantially increase the number of parameters for this purpose.

References

[1] Brodersen, O. & Taupin, K. & Maury, E. & Spieweg, R. & Lieser, J. & Laban, M. & Godard, J. & Vitagliano, P. & Bigot, P. (2005). *Aerodynamic Investigations in the European Project ROSAS (Research on Silent Aircraft Concepts)*. 35th AIAA Fluid Dynamics Conference and Exhibit. 10.2514/6.2005-4891.

[2] Hooker, J.R &, Wick, A & Zeune,C.H.& Agelasto, A. (2013*), Over Wing Nacelle Installations for Improved Energy Efficiency*, 31st AIAA Applied Aerodynamics Conference. June

[3] Fujino, M (2005), Design and Development of the HondaJet, Journal of Aircraft 2005 42:3, 755-764

[4] Wöhler, S & , Hartmann, J & Prenzel, E & Kwik, H., Preliminary Aircraft design for a midrange reference aircraft taking advanced technologies into account as part of the AVACON project for an entry into service in 2028, dglr.de

[5] Lange, F. (2019) High Fidelity Design of the AVACON Research Baseline Aircraft Based on CPACS Data Set, 54th 3AF International Conference on Applied Aerodynamics

[6] Ronzheimer, A. (2012), Aircraft Geometry Parameterization with high-end CAD software for design optimization, Proceedings ECCOMAS

[7] Lange, F & Rudnik,R (2019) Wing Shape Improvement in the Presence of an Over-the-Wing Mounted UHBR Engine for a Short Range Transport Aircraft, AIAA Aviation 2019 Forum, AIAA 2019-2822

[8] Kirz, J.(2019) *Surrogate Based Shape Optimization of a Low Boom Fuselage Wing Configuration*, AIAA Aviation 2019 Forum, AIAA 2019-3489

[9] Gerhold,T. (2005) *MEGAFLOW - Numerical Flow Simulation for Aircraft Design*, vol. 89, ch. Overview of the Hybrid RANS Code TAU, pp. 81–92. Springer-Verlag Berlin Heidelberg, 2005.

[10] Spalart, P. & Allmaras, S. (1992) *A One-Equation Turbulence Model for Aerodynamic Flows* 30th Aerospace Sciences Meeting and Exhibit

[11] Allmaras, S. & Johnson, F. & Spalart, P. (2012) *Modifications and Clarifications for the Implementation of the Spalart-Allmaras Turbulence Model*, Seventh International Conference on Computational Fluid Dynamics (ICCFD7)

[12] Wild, J. (2018) *AeroForce - Thrust/Drag Bookkeeping and Aerodynamic Force Breakdown over Components* update v 0.6.8. DLR-Interner Bericht. DLR-IB-AS-BS-2018-51, 34 S.

[13] G. A. Wilke, G.A. (2017) *Aerodynamic Optimization of Helicopter Rotor Blades using Variable Fidelity Methods*, Ph. D. thesis, Deutsches Zentrum für Luft- und Raumfahrt

[14] Krige, D. (1951) *A statistical approach to some mine valuation and allied problems on the Witwatersrand*, Ph.D. Thesis, University of the Witwatersrand

Appendix

	Drag [C_d *10^5]					
Configuration	Alpha	Nacelle	Wing	Fuselage	Pylon	Overall
WB	1.333		118.74	83.58		202.32
WBE	2.593	-19.77	150.44	107.90		257.11
WBEP	2.805	-10.59	160.00	110.58	-24.47	279.77
WBEPT	3.430	-8.03	138.37	113.36	-20.03	271.50
WBEPTS	3.176	-24.05	139.08	109.73	-21.11	250.20

	Lift [C_l*10^5]			
Configuration	Nacelle	Wing	Fuselage	Pylon
WB		4355.72	653.91	
WBE	73.50	4370.12	584.15	
WBEP	85.04	4301.07	563.03	50.51
WBEPT	141.79	4179.79	565.28	103.17
WBEPTS	111.73	4240.56	578.01	76.64

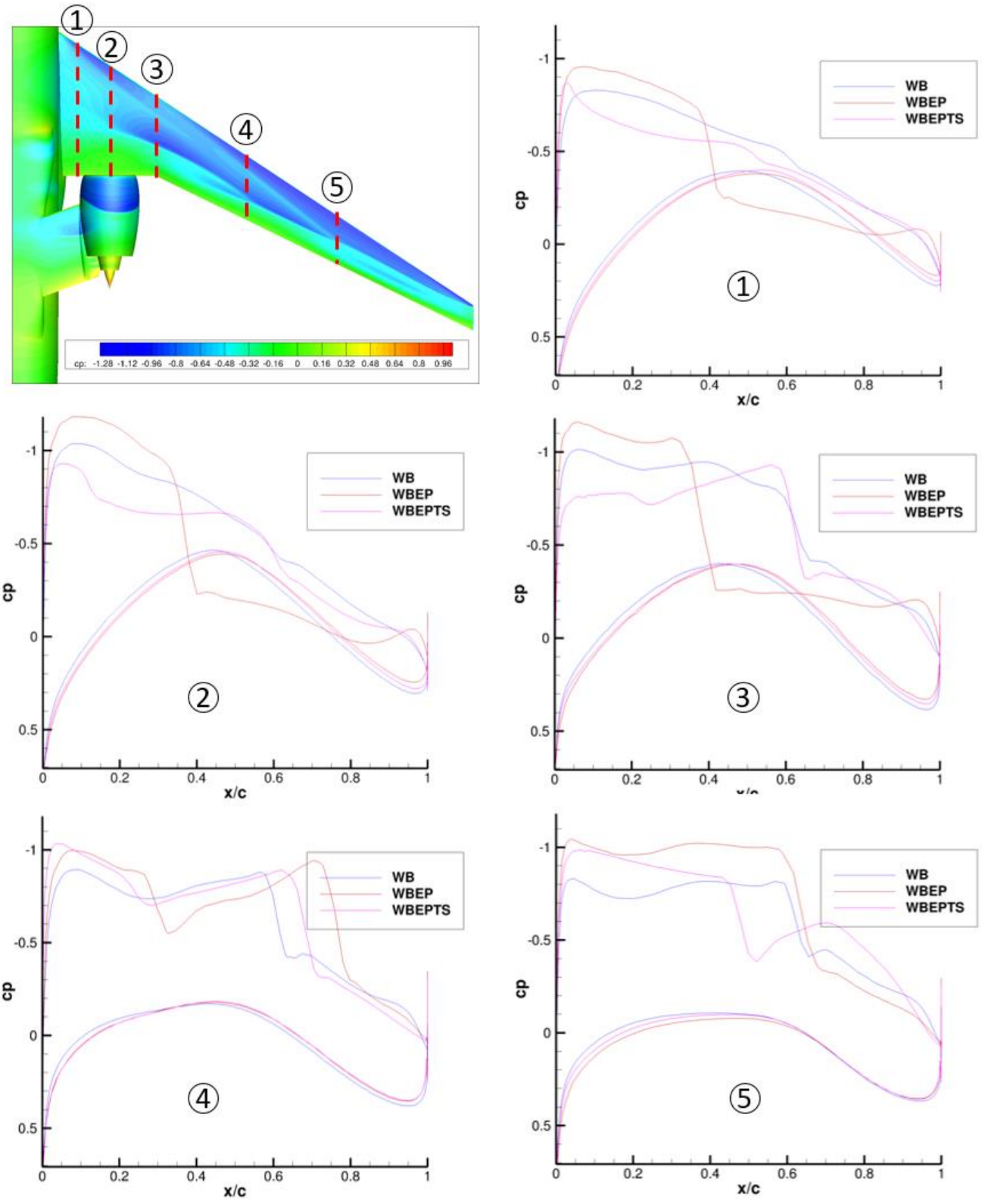

Figure 30 - Pressure distributions in the course of the optimization